Nanoscale

Accepted Manuscript

This article can be cited before page numbers have been issued, to do this please use: X. Zhang, J. Jin, M. Pu, X. Li, X. Ma, P. Gao, Z. Zhao, Y. Wang, C. Wang and X. Luo, *Nanoscale*, 2016, DOI: 10.1039/C6NR07854K.

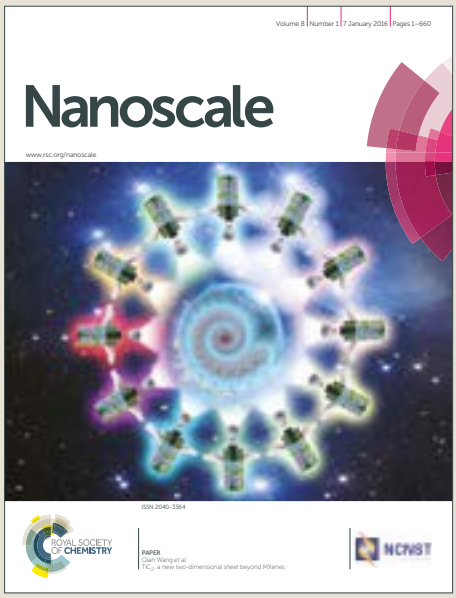

ROYAL SOCIETY OF CHEMISTRY

rsc.li/nanoscale

View Article Online
DOI: 10.1039/C6NR07854K

Journal Name

ARTICLE

Ultrahigh-capacity dynamic holographic display via anisotropic nanoholes

Received 00th January 20xx,
Accepted 00th January 20xx

DOI: 10.1039/x0xx00000x

www.rsc.org/

Xiaohu Zhang,[a,b,#] Jinjin Jin,[a,b,#] Mingbo Pu,[a] Xiong Li,[a] Xiaoliang Ma,[a] Ping Gao,[a] Zeyu Zhao,[a] Yanqin Wang,[a] Changtao Wang,[a] Xiangang Luo*[a]

For the miniaturization of optical holographic and data recording devices, large information capacity or data density is indispensable but difficult to obtain for traditional technologies. In this paper, an ultrahigh-capacity metasurface hologram is proposed by encoding information in deep-subwavelength scale nanoholes array, which can be reconstructed via light beam with proper designed incident angles. The imaging information capacity of the two-dimensional (2D) hologram, defined by the distortion-free region, can be increased to 11.5 times, which is experimentally demonstrated by focused ion beam (FIB) milling an ultrathin metallic film. We also prove the feasibility for three-dimensional (3D) hologram of spiral lines designed by point source algorithm. Benefitting from the ultrahigh capacity of the deep-subwavelength metasurface, dynamic holographic display can be realized by controlling the incident angle. The method proposed here can also be leveraged to achieve large capacity optical storage, colorful holographic display and lithography technology etc.

Introduction

Holography is a technique using the interference pattern between the scattered light of an object and a coherent reference beam to reconstruct the 3D features of the object[1, 2]. Owing to its potential in the cutting-edge optical technologies, holography has enjoyed continuous scientific interest. Traditional holography has scored great achievements and a lot of holographic productions can be found in our daily life. However, the applications of the traditional holography are restricted by the complicated recording process which needs a real object to produce the scattered light, i.e., one cannot get a hologram of a fictitious object. The computer-generated hologram (CGH)[3], which simplifies the recording process by using numerical calculations, is a good method to solve those problems. Using the method of CGH to achieve the hologram and coding the hologram by a certain material/equipment, such as a spatial light modulator (SLM), one can get the hologram of any objects, even though the object is inexistent in the world. But the minimum pixel size of the SLM limits the realization of a bigger viewing angle of the holographic image[4].

Metamaterials are natural candidates for the constitutive materials of the hologram owing to their large flexibilities for controlling the electromagnetic wave on the subwavelength scale. They manipulate the electromagnetic wave with a non-traditional approach. Plentiful novel phenomena and functionalities have been realized with metamaterials, such as negative refraction[5], zero refractive index[6-8], super-resolution imaging[9] and phase/intensity holography[10, 11]. In despite of the achievements of metamaterials in so many new functionalities and the developments of the nanofabrication technology, applying 3D multilayer metamaterials in practical applications is still very inconvenient for the complicated 3D nanofabrication techniques[12]. Luckily, metasurfaces, 2D version of metamaterials consisted of subwavelength structures with various dimensions or orientations[13-17], have been demonstrated to control the properties of electromagnetic wave with relatively low fabrication cost. Different from the phase accumulated in the propagating path through the traditional materials, the phase change introduced by the metasurfaces is correlated with the geometrical parameters such as the dimension and orientation of the structure rather than the thickness of the configurations. Thus a number of researches have been reported, such as vortex beam generator[18-21], metalens[22-24], various holography[25-30], laser beam shaper[31] and helicity dependent surface plasmon polariton excitation[32]. Nevertheless, there are still some problems restricting the widespread application of the metasurfaces. In particular, new applications of holographic technology place greater demands on high information capacity, data density and integration level.

As is well-known, the deep-subwavelength unit cell of the metasurface hologram means the evanescent wave may appear in the hologram's frequency spectrum. But all the previously demonstrated metasurface holograms, to our knowledge, did not use the evanescent wave for far-field imaging. For example, as shown in a previous work[33], only the spectral region between $-0.4k_0$ and $0.4k_0$ is used for the

[a] State Key Lab of Optical Technologies on Nano-Fabrication and Micro-Engineering, Institute of Optics and Electronics, Chinese Academy of Sciences, P.O. Box 350, Chengdu, 610209, China. E-mail: lxg@ioe.ac.cn.
[b] University of Chinese Academy of Sciences, Beijing 100049, China.
[#] These authors contributed equally to this work.

holographic image even though the spatial spectrum range of the hologram is larger than $-k_0$ to k_0. In other words, so much information is discarded in current metasurface holographic technology. In this paper, the off-axis illumination is proposed to increase the information capacity by transferring the evanescent wave into the propagating wave. The metasurface hologram is designed with variant-orientations elongated nanoapertures, which possesses great advantages in holography for its high tolerance to fabrication errors[33]. The evanescent wave information of normal incidence has been used for holographic image in the Fraunhofer region of the 2D metasurface hologram via off-axis illumination, which is different from some demonstrated holographic imaging, such as the high flexibility for incidence angles of meta-hologram[34] and wide-angle reflection holography[35]. Moreover, this method for increase of the imaging information capacity is also applicable for 3D hologram, which has been proved with experiments of 3D spiral line. Furthermore, dynamic holographic display can be achieved with variant incident angles.

The principle for the increment of the imaging information capacity

The schematic of the imaging information capacity's increment is shown in Figure 1. When the light normally incidents on the sample, as shown by the green color light, the holographic image in the Fraunhofer region can be expressed as: $G(f_x,f_y)=F(g(x,y))$, where (x,y) represents the coordinate of the metasurface hologram, (f_x,f_y) is the coordinate in the corresponding frequency spectrum ($f_x=k_x/(\lambda k_0)$, $f_y=k_y/(\lambda k_0)$), the $g(x,y)$ describes the electromagnetic field just after the sample and F means the fast Fourier-transform algorithm. When the light incidents on the metasurface hologram with an angle $\theta(\theta_x,\theta_y,\theta_z)$, the related far field image can be written as:

$$G(f_x - \cos(\theta_x)/\lambda, f_y - \cos(\theta_y)/\lambda) = F\{g(x,y)\exp[i\,2\pi(x*\cos(\theta_x) + y*\cos(\theta_y))/\lambda]\}, \quad (1)$$

where θ_x and θ_y indicate the angles between the incident orientation and the positive directions of the x axis, y axis, respectively. As shown in equation (1), varying incident angle could lead to the displacement of the frequency spectrum. It means that every part of the frequency spectrum can be transferred to anywhere by providing the corresponding incident light with a specific phase distribution. It's an interesting phenomenon that when illuminating the sample with an oblique angle, the Africa part changes from the down-left region of the world map (green map) to the central (red map), but the American part seems to be changing from right-down region to the left, as shown in Figure 1. This is caused by that the hologram is pixelated into discrete pixels rather than continuous hologram. Mathematically, the whole frequency spectrum of the pixel hologram can be expressed as:

$$G_w(f_x, f_y) = \sum_{m=-\infty}^{\infty}\sum_{n=-\infty}^{\infty} G(f_x - m/p, f_y - n/p)$$

, where m and n are integers, p is the period of the square pixels of the meta-hologram. This equation implies the whole frequency spectrum is periodic and its unit cell is the green/red map shown in Figure 1. So the American part (red map in Figure 1) is not the corresponding part of green map, but the homologous part of another unit cell of the whole frequency spectrum. Based on the periodic property of the whole frequency spectrum of the pixel hologram, it is enough to investigate only one unit cell, as the green/red map shown in Figure 1. Theoretically, the range for k_x/k_0 or k_y/k_0 is from $-\lambda/2p$ to $\lambda/2p$, where the λ is the wavelength of the light. It signifies that the angular spectrum is composed of the propagating wave and the evanescent wave when p is smaller than half of the λ, as shown in Figure 1. For the normal incidence light, the wave vector in region (A) cannot radiate to Fraunhofer region, so using the information in the region (A) for 2D holographic imaging is impossible normally. Owing to the geometric relationship, the θ_x, θ_y and θ_z satisfy the relational expression: $\cos^2(\theta_x)+\cos^2(\theta_y)+\cos^2(\theta_z)=1$. When k_z ($k_z = k_0\cos(\theta_z)$) is a real, we can obtain the relation:

$$\cos^2(\theta_x) + \cos^2(\theta_y) \le 1 \quad (2)$$

With equation (1) and equation (2), one can conclude that the wave vector in a circular area with radius of $2k_0$ can be transferred into the propagating wave field of the frequency spectrum. So the maximal increasing quantity for the imaging information capacity should be the ratio of those circular areas with radius $2k_0$ to k_0. It means the information capacity for far-field imaging of a certain hologram, which can be regard as the data density, can be increased to 4 times.

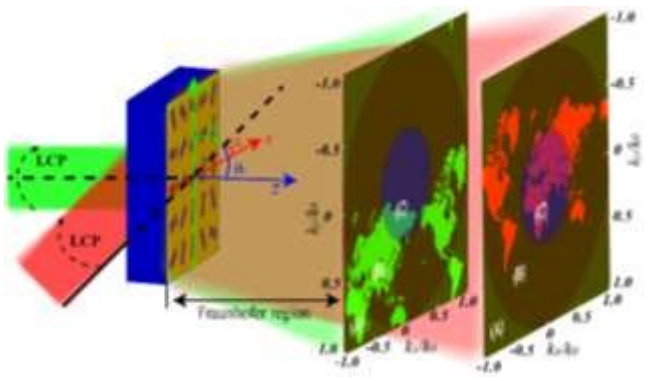

Figure 1. The green color represents the light normal impinging on the sample and the red color means the light incidence on the hologram with an oblique angle $\theta(\theta_x,\theta_y,\theta_z)$, where θ_x, θ_y and θ_z are the angles between the incident orientation and the positive directions of x axis, y axis, z axis, respectively. The three regions signed in the frequency spectrum with different color mean: (A) evanescent wave region; (B) distortion region; (C) distortion-free region. The incident wavelength is 405 nm.

Taking the practical situation into account, the screen of the holographic image is always a charge coupled device (CCD) or some other flat planes. It is impossible for a flat screen to get all the transmissive wave information in a hologram consisted of deep-subwavelength structures. The receivable range for k_x/k_0 or k_y/k_0 is confined by the limited size of the screen. On the other hand, the image geometrical distortion will appear when the bound of the k_x/k_0 or k_y/k_0 is beyond the paraxial approximation due to the difference between the area space and the frequency space[27]. Here, the discrepancy of 10% is used to distinguish the boundary between distortion region and distortion-free region. Theoretically, the discrepancy could be depicted as:

$$\frac{\tan(\theta_z') - \sin(\theta_z')}{\sin(\theta_z')} \leq 10\% \quad , \qquad (3)$$

where θ'_z denotes the angle between the emitting direction and the positive direction of the z axis. From equation (3), it concludes that $|\sin(\theta'_z)| \leqslant 0.417$. Due to the geometric relation $\left|\sin(\theta_z')\right| = \sqrt{(k_x/k_0)^2 + (k_y/k_0)^2}$, the distortion region (B) and the distortion-free region (C) can be confirmed, as shown in Figure 1. Moreover, the region (C) contains the usable information for 2D holographic imaging. It should be noted that the pre-compensated algorithm can eliminate the image distortion[27], but the distances of the controllable nearest neighbors between the paraxial region and non-paraxial region of the holographic image are different. This difference would make the resolution of the image's central and edge area nonuniform, so the pre-compensated algorithm is not a good scheme to achieve a good image with the large field of view. Theoretically, the information capacity of the meta-hologram is dependent on the quantity of the pixels in the sample. But the information in the evanescent wave region and distortion region is unusable for high quality image, only the distortion-free region information can be used for imaging conveniently. With equations (1-3), the maximal increment of the usable information capacity, defined by the distortion-free region, is $(1.417k_0/0.417k_0)^2$ under off-axis illumination, i.e., the usable information capacity of a certain hologram can be increased to as high as 11.5 times.

Design and characterization of the metasurface hologram

In order to validate the scheme proposed in this paper, the phase hologram of a preset world map is obtained by utilizing the iterative Fourier-transform algorithm (IFTA)[36] and verified with Fraunhofer diffraction formula (Figure 2a). The elongated nanoaperture composed of Au film on SiO_2 substrate is used as the unit cell of the metasurface hologram, as shown in Figure 2b. The thicknesses of the Au film and SiO_2 are 120 nm and 2 mm, respectively. The elongated aperture could rotate in the x-y plane with an orientation angle φ to produce a certain phase delay. The phase change is occurred when the incident circularly polarized (CP) light converts to its opposite helicity when it transmits through the metasurface. Theoretically, the phase change can be depicted as: $\phi=2\sigma\varphi$, where $\sigma=\pm1$ denotes the incident/transmitted polarization. '+1' means the left-handed circular polarization (LCP)/right-handed circular polarization (RCP) and '-1' signs for RCP/LCP[37]. As the phase change is twice of the orientation angle of the elongated nanoaperture and its

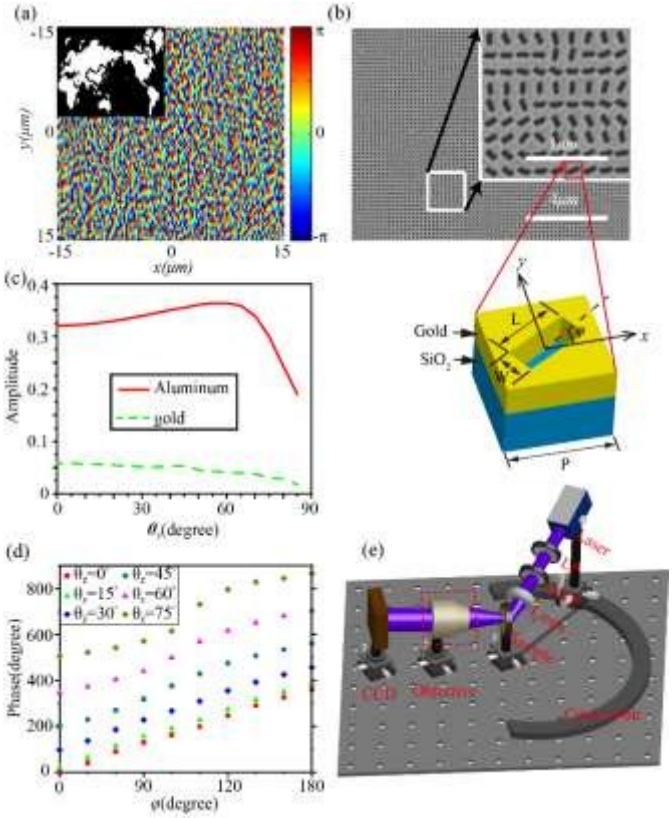

Figure 2. (a) The designed phase hologram with 150×150 pixels for the world map shown in the inset. (b) The scanning electron microscope (SEM) image of part of the fabricated metasurface hologram and the corresponding scale bar is 4 μm. The higher resolution ratio SEM image is shown in the up-right inset with scale bar 1 μm. The unit cell adopted is also shown in the figure with the size: P=200 nm (period), L=140 nm (length), W=60nm (width), φ: the orientation angle of the nanoaperture, the thickness of the quartz substrate is 2 mm in the experiment. (c) Conversion amplitude versus the incident angle θ_z (θ_y=90°) (The red line and green dash line are related to the structure with Aluminum and gold, respectively). (d) Phase shift with different incidence angle θ_z (θ_y=90°) and orientation angle φ. (e) The optical set-up for the observation of the holographic images with tunable incident angle. The objective in the red dashed line is placed for the reconstruction of the 3D holographic image.

orientation angle can be set from 0 to 180 degree, the phase could be modulated from 0 to 360 degree easily. In addition, the transmission efficiency change is so little with the change of the nanoaperture's orientation angle from 0 to 180 degree that the scattering amplitude can be regard as a uniform value[22]. Those above characteristics ensure the elongated nanoaperture can be used to realize the phase hologram. Figure 2c-d show the average conversion amplitude and phase shift for the RCP light under different incidence angle of LCP

View Article Online
DOI: 10.1039/C6NR07854K

light and orientation angle of the nano-aperture, respectively. The broadband property of the structure can be found in a previous work[22] of our team. In theory, if the incidence wavelength larger than twice of the period of the structure (>400nm), the evanescent wave will appear in the frequency spectrum. But the larger of the incidence wavelength, the more evanescent wave information appear in the frequency spectrum, which is difficult to reconstructed with the restricted incidence angle we can used in the experiment. So the light of wavelength 405nm is used as the incidence source both the simulation and experiment. As shown in Figure 2c, the conversion efficiency of the structure with gold (green dash line) is very low, which can be solved with high-sensitivity detector and high-power laser source in the experiment. In addition, the reflectarrays metasurface[26] and dielectric metasurface[38] can increase the conversion efficiency. The efficiency can also be improved by using Aluminum instead of gold, which is shown in Figure 2c (red line). Figure 2d shows the phase shift is approximately linear to φ with incidence angle θ_z introducing a constant phase shift, which will not influence the holographic image (Some deviation of the linear relation between the phase shift and φ will not affect the holographic image seriously for the tolerance of the phase hologram[33]). So the hologram can be designed with normal incidence light and measured with some other incidence angles, only introducing displacements for the frequency spectrum, as equation (1) implied.

The hologram is coded with the elongated nanoaperture structure according to the ϕ-φ relation. Then, the metasurface hologram is fabricated with FIB in an area of 30 μm×30 μm. The scanning electron microscope (SEM) image is shown in Figure 2b. Furthermore, the experimental setup for the off-axis illumination shown in Figure 2e is used to experimentally characterize the performance of the fabricated sample. The laser source at wavelength 405 nm is placed on a five-dimensional translation stage whose orientation angle in horizontal/vertical direction and height can be adjusted. The stage is put on a circle orbit so that the laser can move with a decided distance in the horizontal plane to produce a certain incident angle. The hologram sample is mounted on the center of the circle orbit. The linear polarizer (LP) and quarter wave plate (QWP) in front of the sample are used to generate the desired CP light. To enhance the power of the incident light for the sample with micron size, a lens with focal length at 5 cm is placed in front of the sample to focus the CP light. The holographic image scattered by the metasurface is collected with a CCD. The objective after the sample is used to magnify the holographic image in the following experiment of 3D holographic metasurface sample. Theoretically, with the using of the off-axis illumination, the useful holographic image is separated from the zero order of the incident light. Then

View Article Online
DOI: 10.1039/C6NR07854K

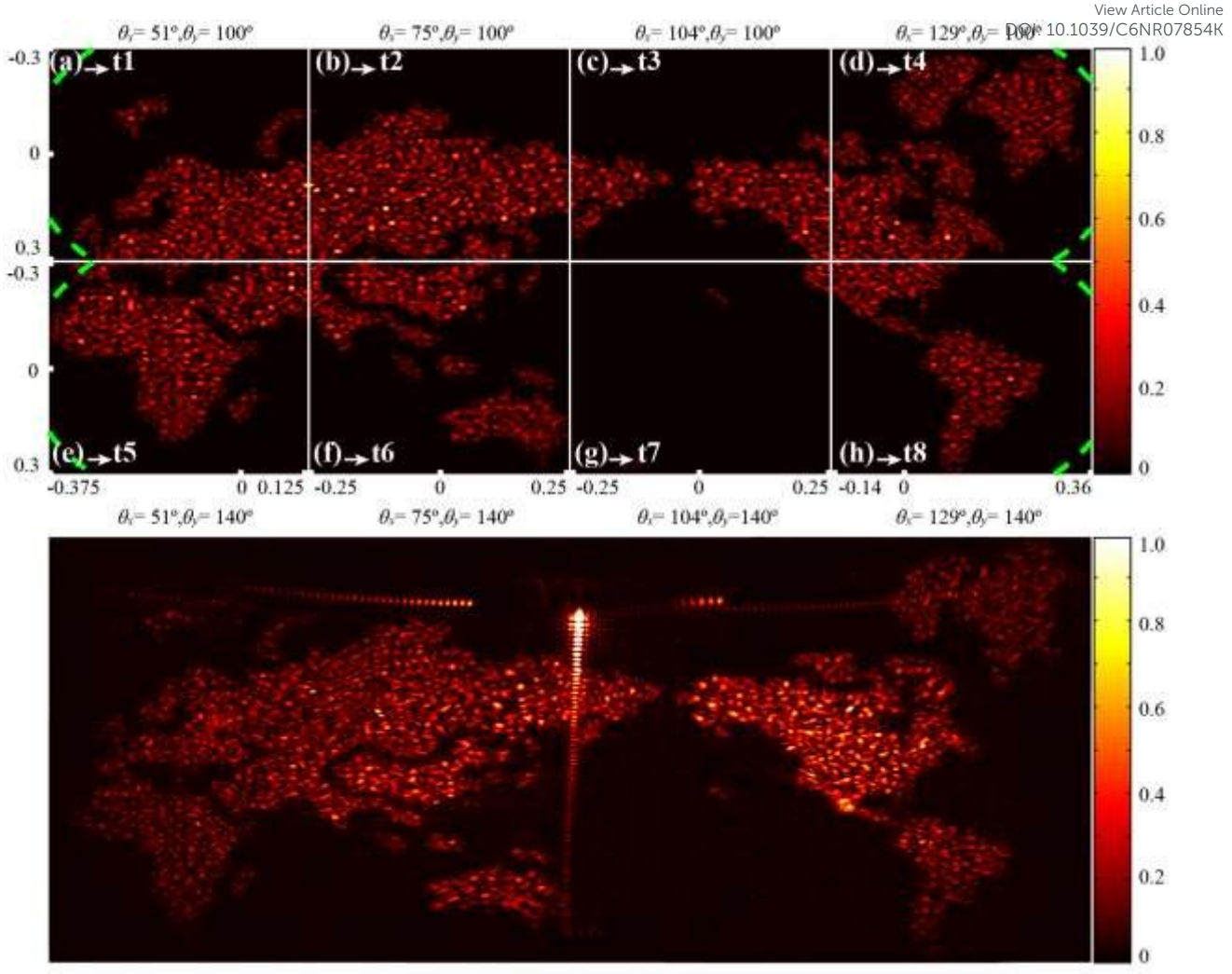

Figure 3. (a)-(h) the simulation results with eight groups of incident angles, which are related to different time. The green dashed lines in (a), (d), (e) and (h) denote the boundaries between the distortion region and distortion-free region. (i) The stitched holographic image of experimental results with different incident angles. The incident wavelength is 405 nm**.** The intensity has been normalized.

compared to other 2D or 3D metasurface holographic experiments[25, 33], this optical setup does not need a pair of QWP and LP after the sample to filter the CP light without cross- polarization. As a consequence, the method of off-axis illumination can simplify the experimental setup.

The simulated holographic images are shown in Figure 3a-h. The whole simulated image's profile is accord with the preset world map (inset of Figure 2a), which demonstrates the effectivity of the design method. The quality of the holographic image can be optimized with larger sample which can be fabricated through electron beam lithography (EBL)[26, 27]. In experiment, due to the limited photosensitive area of the CCD, the whole world map image cannot be directly recorded. Moreover, as described in the principle part, the distortion-free region (Figure 1) is a circular area with radius of $0.417k_0$ in the frequency spectrum, so several measurement windows with all the corresponding images in the distortion-free region are used in the experiment, even though the world map is an entire target image shown in inset of Figure 2a in the design. Namely, the hologram is related to a single phase profile for the whole world map rather than 8 phase profiles for Figure 3a-h. As shown in Figure 3a-h, eight groups of incident angles (θ_x,θ_y): (51°,100°), (75°,100°), (104°,100°), (129°,100°), (51°,140°), (75°,140°), (104°,140°), (129°,140°), which are associated with t1-t8, are adopted in the simulation. A video which contains eight frames can be theoretically attained in the case of real-time varying the incident angles. More incident angles are employed for the limited photosensitive area of the used CCD in our experiment. After measuring the every part of the image, the experimental pictures are spliced into an overall world map image, as shown in Figure 3i. For the incident angles shown in Figure 3e and Figure 3h, we can conclude θ_z=82.5° for the relation: $\cos^2(\theta_z)=1-\cos^2(51°)-\cos^2(140°)$, which is near glancing incidence in the experiment ($\sin(\theta_z)$=0.99). Those incidence angles show some evanescent wave information of normal incidence has been transferred into the distortion-free region, which prove the scheme of

View Article Online
DOI: 10.1039/C6NR07854K

using the evanescent wave information for imaging in the far-field proposed in this paper.

Obviously, the profile of the intensity distribution obtained by experiment is in very good agreement with the simulation result. It should be noted that the intensity distribution of the whole image, both the simulation and experiment, is not smooth enough. This is caused by the appearance of the

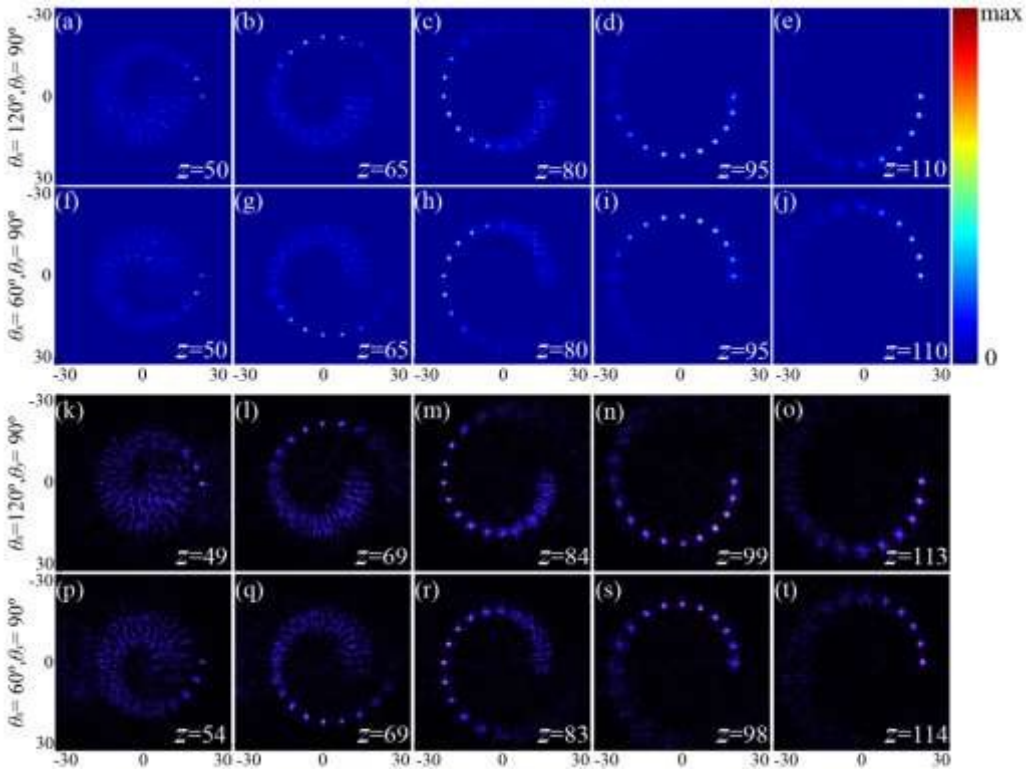

Figure 4. (a)-(e) the simulation results with different distances in z-axis with incident angle: θ_x=120°,θ_y=90°. (f)-(j) the corresponding simulation results with θ_x=60°,θ_y=90°. The scale bar has been uniformed. (k)-(o),(p)-(t) the experimental results relative to (a)-(e) and (f)-(j). The incident wavelength is 405 nm. The unit is μm.

speckle pattern, which can be further optimized by a N×N (N is an integer) periodic hologram design based on the concept of the Dammann gratings[26, 39]. As seen in Figure 3i, because the conversion efficiency will reduce versus the increasing of the incidence angle, the fringe regions, such as the Africa, Europe and South America, are much dimmer than the central region of the world-map, which is matched with the simulation result of Figure 2c. In addition, with using the off-axis illumination, a majority of horizontal line of the zero order is separated from the image to eliminate its influence on the holographic image, which demonstrates that the method of off-axis illumination can simplify the optical setup of metasurface hologram experiment. But restricted by the incidence angle we used in the design and experiment, we cannot separate the whole zero-order pattern from the image, which can be optimized with larger incidence wave vector, even using the evanescent wave as the illuminating source. Consequently, one can find that the experimental results are matched with simulation results except some stitched traces.

It is important to note that the above method is also effective for 3D holography. The usable information capacity for 3D hologram can be defined with the divergent angle of the emergent light from the sample, which is similar to the case of 2D hologram. In the following, a 3D metasurface hologram is experimentally demonstrated. The hologram is generated with point source algorithm and the correctness of the design is verified through the Fresnel diffraction theory. For achieving a more uniform amplitude 3D CGH, the Gaussian distributed pseudorandom phase X~2π*N(μ,ξ2), with μ=0 and ξ=1, is added to each point source. After calculated the holograms of right spiral line and left spiral line, the corresponding phase shifts (exp(i2π$x$cos(60°)/λ); exp(i2π$x$cos(120°)/λ)) are added to each hologram. And the final phase hologram is the phase part of the superimposition of those two complex amplitudes. The coding method and fabrication strategy of the 3D hologram are same with the 2D hologram. Figure 4a-e show the simulation results of different distances in z-axis with the incident angle of θ_x=120°, θ_y=90°. A clear right spiral line is obtained with the increase of the distance. Otherwise, the left spiral line is realized with the incident angle of θ_x=60°, θ_y=90° (Figure 4f-j).

In order to conveniently characterize the metasurface hologram, a ×100 magnification objective lens (Figure 2e) is adopted in the measurement system to magnify the spiral line whose diameter is 40 μm. Several transections of the 3D spiral line are obtained by gradually tuning the distance between the sample and the objective to demonstrate the 3D characteristic of the spiral line. Through a series of 2D results with the depth information of the 3D images, the 3D feature

of the holographic images is verified. The corresponding experimental results with the incident angle θ_x=120°, θ_y=90° and θ_x=60°, θ_y=90° are shown in Figure 4k-o and Figure 4p-t, respectively. The experimental results are perfectly matched with the simulation results except some experimental errors of the distance in *z*-axis. As shown in Figure 4k-t, the experimental results are very clear and unambiguously indicate that the scheme for increasing the imaging information capacity adopted here is feasible for 3D holography.

Conclusions

The increase of the usable information capacity is crucial for decreasing the size of the functional device and reducing the fabrication expense of a certain hologram. As described above, the imaging information capacity of 2D hologram is 4 times to its propagating wave region and 11.5 times compared with the distortion-free region via off-axis illumination. The limiting condition described in equation (2) will be broken when we illuminate the hologram with evanescent wave and the usable data density will be further increased using higher-order evanescent wave. For example, the imaging information capacity will be increased to 9 times corresponding to the propagating wave region and 33.6 times to the distortion-free region with an incident wave vector of 0-2k_0 rather than 0-k_0. In the 3D holographic experiment, we just used two holograms with respective phase shift to generate the designed phase hologram and achieved perfectly matched experimental results.

In summary, we propose and experimentally verify a method increasing the imaging information capacity of the 2D/3D metasurface hologram with off-axis illumination. A 2D metasurface hologram using the information in the evanescent wave region to image in the Fraunhofer region is designed based on the scheme. The imaging information capacity determined by the distortion-free region, which can be regard as the data density, is increased to 11.5 times. The dynamic display can be achieved with real-time controlling of the incident angles. In addition, the increase of the usable imaging information capacity through off-axis illumination is also proved with 3D holographic experiment. Furthermore, the method of off-axis illumination will simplify the experimental set-up for the separation of the zero order diffraction light and the holographic image. Such a scheme could potentially be applied in colourful holographic display, optical information processing and holographic storage etc.

Acknowledgements

This work was supported by 973 Program of China (No. 2013CBA01700), the National Natural Science Foundation of China (61138002, 61575201).

Notes and references

1. D. Gabor, *Nature*, 1948, **161**, 777.
2. E. N. Leith and Upatniek.J, *J. Opt. Soc. Am.*, 1962, **52**, 1123-1130.
3. C. Slinger, C. Cameron and M. Stanley, *Computer*, 2005, **38**, 46-53.
4. X. Li, H. Ren, X. Chen, J. Liu, Q. Li, C. Li, G. Xue, J. Jia, L. Cao, A. Sahu, B. Hu, Y. Wang, G. Jin and M. Gu, *Nat. Commun.*, 2015, **6**, 6984.
5. J. Valentine, S. Zhang, T. Zentgraf, E. Ulin-Avila, D. A. Genov, G. Bartal and X. Zhang, *Nature*, 2008, **455**, 376-379.
6. X. Yang, C. Hu, H. Deng, D. Rosenmann, D. A. Czaplewski and J. Gao, *Opt. Express*, 2013, **21**, 23631-23639.
7. R. Maas, J. Parsons, N. Engheta and A. Polman, *Nat. Photonics*, 2013, **7**, 907-912.
8. Y. C. Jun, J. Reno, T. Ribaudo, E. Shaner, J. J. Greffet, S. Vassant, F. Marquier, M. Sinclair and I. Brener, *Nano Lett.*, 2013, **13**, 5391-5396.
9. Z. Liu, H. Lee, Y. Xiong, C. Sun and X. Zhang, *Science*, 2007, **315**, 1686.
10. S. Larouche, Y. J. Tsai, T. Tyler, N. M. Jokerst and D. R. Smith, *Nat. Mater.*, 2012, **11**, 450-454.
11. H. Butt, Y. Montelongo, T. Butler, R. Rajesekharan, Q. Dai, S. G. Shiva-Reddy, T. D. Wilkinson and G. A. Amaratunga, *Adv. Mater.*, 2012, **24**, OP331-336.
12. N. Meinzer, W. L. Barnes and I. R. Hooper, *Nat. Photonics*, 2014, **8**, 889-898.
13. N. Yu, P. Genevet, M. A. Kats, F. Aieta, J. P. Tetienne, F. Capasso and Z. Gaburro, *Science*, 2011, **334**, 333-337.
14. M. Pu, X. Li, X. Ma, Y. Wang, Z. Zhao, C. Wang, C. Hu, P. Gao, C. Huang, H. Ren, X. Li, F. Qin, J. Yang, M. Gu, M. Hong and X. Luo, *Sci. Adv.*, 2015, **1**, e1500396.
15. Z. Zhao, M. Pu, H. Gao, J. Jin, X. Li, X. Ma, Y. Wang, P. Gao and X. Luo, *Sci. Rep.*, 2015, **5**, 15781.
16. X. Luo, *Sci. China-Phys. Mech. Astron.*, 2015, **58**, 594201.
17. J. Luo, B. Zeng, C. Wang, P. Gao, K. Liu, M. Pu, J. Jin, Z. Zhao, X. Li, H. Yu and X. Luo, *Nanoscale*, 2015, **7**, 18805-18812.
18. E. Karimi, S. A. Schulz, I. De Leon, H. Qassim, J. Upham and R. W. Boyd, *Light-Sci. Appl.*, 2014, **3**, e167.
19. P. Genevet, N. F. Yu, F. Aieta, J. Lin, M. A. Kats, R. Blanchard, M. O. Scully, Z. Gaburro and F. Capasso, *Appl. Phys. Lett.*, 2012, **100**, 013101.
20. X. Ma, M. Pu, X. Li, C. Huang, Y. Wang, W. Pan, B. Zhao, J. Cui, C. Wang, Z. Zhao and X. Luo, *Sci. Rep.*, 2015, **5**, 10365.
21. K. P. Yang, M. B. Pu, X. Li, X. L. Ma, J. Luo, H. Gao and X. G. Luo, *Nanoscale*, 2016, **8**, 12267-12271.
22. D. L. Tang, C. T. Wang, Z. Y. Zhao, Y. Q. Wang, M. B. Pu, X. Li, P. Gao and X. G. Luo, *Laser Photon. Rev.*, 2015, **9**, 713-719.
23. Y. Chen, X. Li, Y. Sonnefraud, A. I. Fernandez-Dominguez, X. Luo, M. Hong and S. A. Maier, *Sci. Rep.*, 2015, **5**, 8660.
24. X. J. Ni, S. Ishii, A. V. Kildishev and V. M. Shalaev, *Light-Sci. Appl.*, 2013, **2**, e72.
25. L. L. Huang, X. Z. Chen, H. Muhlenbernd, H. Zhang, S. M. Chen, B. F. Bai, Q. F. Tan, G. F. Jin, K. W. Cheah, C. W. Qiu, J. S. Li, T. Zentgraf and S. Zhang, *Nat. Commun.*, 2013, **4**, 2808.
26. G. Zheng, H. Muhlenbernd, M. Kenney, G. Li, T. Zentgraf and S. Zhang, *Nat. Nanotechnol.*, 2015, **10**, 308-312.
27. D. Wen, F. Yue, G. Li, G. Zheng, K. Chan, S. Chen, M. Chen, K. F. Li, P. W. Wong, K. W. Cheah, E. Y. Pun, S. Zhang and X. Chen, *Nat. Commun.*, 2015, **6**, 8241.
28. D. D. Wen, S. M. Chen, F. Y. Yue, K. L. Chan, M. Chen, M. Ardron, K. F. Li, P. W. H. Wong, K. W. Cheah, E. Y. B. Pun, G. X. Li, S. Zhang and X. Z. Chen, *Adv. Opt. Mater.*, 2016, **4**, 321-327.
29. L. Huang, H. Muhlenbernd, X. Li, X. Song, B. Bai, Y. Wang and T. Zentgraf, *Adv. Mater.*, 2015, **27**, 6444-6449.
30. Y. W. Huang, W. T. Chen, W. Y. Tsai, P. C. Wu, C. M. Wang, G. Sun and D. P. Tsai, *Nano lett.*, 2015, **15**, 3122-3127.
31. X. Z. Chen, Y. Zhang, L. L. Huang and S. Zhang, *Adv. Opt. Mater.*, 2014, **2**, 978-982.

View Article Online
DOI: 10.1039/C6NR07854K

32. L. L. Huang, X. Z. Chen, B. F. Bai, Q. F. Tan, G. F. Jin, T. Zentgraf and S. Zhang, *Light-Sci. Appl.*, 2013, **2**, e70.
33. X. Zhang, J. Jin, Y. Wang, M. Pu, X. Li, Z. Zhao, P. Gao, C. Wang and X. Luo, *Sci. Rep.*, 2016, **6**, 19856.
34. W. T. Chen, K.-Y. Yang, C.-M. Wang, Y.-W. Huang, G. Sun, I. D. Chiang, C. Y. Liao, W.-L. Hsu, H. T. Lin, S. Sun, L. Zhou, A. Q. Liu and D. P. Tsai, *Nano lett*., 2014, **14**, 225-230.
35. Y. Yifat, M. Eitan, Z. Iluz, Y. Hanein, A. Boag and J. Scheuer, *Nano lett.*, 2014, **14**, 2485-2490.
36. R. W. Gerchberg and W. O. Saxton, *Optik*, 1972, **35**, 237.
37. X. Chen, L. Huang, H. Muhlenbernd, G. Li, B. Bai, Q. Tan, G. Jin, C. W. Qiu, S. Zhang and T. Zentgraf, *Nat. Commun.*, 2012, **3**, 1198.
38. K. Huang, Z. Dong, S. Mei, L. Zhang, Y. Liu, H. Liu, H. Zhu, J. Teng, B. Luk'Yanchuk, J. K. W. Yang and C. -W. Qiu, *Laser Photon. Rev.*, 2016, **10**, 500–509.
39. H. Dammann and K. Gortler, *Opt. Commun.*, 1971, **3**, 312-315.